RESEARCH PAPER



Magneto-Bioconvection Dynamics of Synovial Nanofluids: Consequences of Porosity, Rheology, and Heat Generation

Shaimaa Fathey Ramadan a , M. M. Bhatti $^bc, ^*$, Khaled Saad Mekheimer d , Ali Mohamed Ali Soliman Moawad d , C. M. Khalique b

^a Mathematical Department, Faculty of Science (Girls), Al-Azhar University, Nasr City, Cairo, Egypt

^b Material Science Innovation and Modelling (MaSIM) Research Focus Area, North-West University (Mafikeng Campus),

Private Bag X2046, Mmabatho 2735, South Africa

Abstract

The primary objective of this study is to analyze the thermal processes, nanoparticle concentration, and bioconvection mechanisms in a synovial fluid model using numerical methods. Two fluid models are considered: Model (1), representing a shear-thinning fluid, and Model (2), representing a shear-thickening fluid. The influences of magnetic field, porosity, Joule heating, and viscous dissipation are incorporated into the analysis. The governing equations for momentum, energy, nanoparticle concentration, and motile microorganism density have formulated using the lubrication approximation. The resulting nonlinear differential equations are solved numerically using the Runge-Kutta-Merson method and the finite difference scheme. The effects of key parameters on velocity, temperature, nanoparticle concentration, and motile microorganism density are systematically explored. The study reveals that the magnetic field significantly alters the fluid motion, reducing velocity as magnetic intensity increases, whereas higher velocities are observed in the shear-thinning model. The synovial fluid achieves its maximum velocity near the knee cartilage surface. The temperature profile is higher in Model (1) than in Model (2), primarily due to heat generation effects. The concentration production parameter also affects the thermal field, leading to lower nanoparticle concentrations in Model (1). Moreover, the thermophoretic parameter decreases nanoparticle concentration, while the Brownian motion parameter enhances it. Heat-source-driven fluid motion ultimately reduces the density of motile microorganisms.

Keywords: Synovial fluid; Bioconvection; nanoparticles; microorganisms; FDM.

1. Introduction

The thermal characteristics of fluids play a significant role in cooling and heating applications across various engineering fields. Conventional heat-transfer fluids often fail to meet industrial and technical requirements for high cooling efficiency due to their inherently low thermal conductivity. In recent years, researchers have sought to enhance thermal performance by dispersing tiny nanoparticles into base fluids [1]. However, the early attempts to suspend nanoparticles were largely ineffective because of issues such as particle sedimentation, excessive pressure drops, corrosion of equipment, particle agglomeration (clogging), and inadequate thermal conductivity.

To address these limitations, researchers focused on reducing the size of the solid particles to achieve the desired thermal properties. These efforts led to the development of nanofluids, a concept rooted in engineering at the nanoscale. Various chemical and physical techniques have been employed to reduce particle sizes to the order of 10-9 meters. As a result, nanofluids have been

* Corresponding author. Tel.: +86-17660692869. E-mail address: Bhatti.bhatti@nwu.ac.za

^c Department of Physics, College of Science, Korea University, 145 Anam-ro, Seongbuk-gu, Seoul 02841, Republic of Korea ^d Mathematical Department, Faculty of Science (Girls), Al-Azhar University, Nasr City, Cairo, Egypt

engineered at the atomic scale to exhibit superior thermal behavior compared to fluids with larger particles. Choi [2] and Lee [3] introduced nanofluids—colloidal suspensions of nanoparticles—and demonstrated their enhanced thermal properties and improved efficiency in a wide range of applications.

Nanoparticles are now synthesized from diverse materials, including gold, magnesium, silver, copper, carbon nanotubes, semiconductors, nitride ceramics, and oxide ceramics. Nanofluids may consist of either Newtonian or non-Newtonian base fluids combined with different types of nanoparticles. Their primary purpose is to improve thermal properties while minimizing particle volume fraction by achieving effective dispersion and distribution within the fluid. Nanofluids can enhance key physical properties such as mass diffusivity, thermal diffusivity, and viscosity, which are generally superior to those of base fluids like oil or water [4]. Consequently, nanofluids have extensive applications in detergency, biomedia sterilization, computer and electronics cooling, fuel cooling, automotive thermal systems, and transformer cooling. They also offer the potential for ultra-high-performance heating and cooling in industrial processes such as aircraft propulsion ducts, solar collectors, vehicle radiators, semiconductor fabrication, and nuclear reactor thermal management.

Imran et al. [5] investigated the interaction between cilia and nanoparticles in a biological fluid flowing through a duct. Eid [6] analyzed the dynamics of differently shaped nanoparticles suspended in a Sisko biological fluid under convective conditions. Elelamy et al. [7] studied blood flow, considering non-Newtonian behavior, magnetic effects, slip conditions, and heat transfer, and further examined bacterial development near coronary valves. Bhatti et al. [8] examined the biological rheology of a Williamson fluid under magnetic and convective effects and explored entropy generation. Elangovan et al. [9] analytically examined the movement of a magnetized nanofluid containing TiO₂-Fe₃O₄ nanoparticles with slip effects. Sharma et al. [10] performed a comprehensive analysis of magnetized fluid flow over an elastic surface influenced by chemical reactions and thermal radiation, accounting for Brownian motion and thermophoresis. Raza et al. [11] developed a mathematical model for the flow of biological nanofluids through a porous medium containing carbon nanotubes.

Bioconvection is a natural process observed in certain microorganisms. When microorganisms are denser than the surrounding fluid, they tend to swim upward; once a sufficiently dense layer forms at the top, they sink, creating bioconvective patterns. Oxytactic bacteria such as *Bacillus subtilis* migrate toward regions with higher oxygen concentrations, and oxygen is replenished through surface diffusion [12]. Engineers have recently explored combining nanoparticles with motile microorganisms to regulate heat and mass transfer in industries such as coatings, bioreactors, and fuel cells. This combined phenomenon is known as nano fluid bioconvection, and the resulting fluids are referred to as bio-nanofluids [13]. The bioconvection mechanism is relevant in many biological processes and micro-devices, as the motion of microorganisms enhances mixing, reaction rates, and transport processes. Using self-propelled microorganisms can significantly improve convective transport and facilitate controlled mixing. Adding microorganisms to engineered fluids can also enhance the effectiveness of magnetohydrodynamic coating processes. This approach can be applied to various substrate geometries, including flat plates, parallel plates, curved surfaces, and wedge-shaped structures. Basha and Sivaraj [14] numerically investigated blood flow with nanoparticles in several geometrical configurations, emphasizing circulatory system behavior.

Researchers have further examined the simultaneous influence of magnetic fields in nanofluid bioconvection systems—referred to as magnetohydrodynamic nanofluid bioconvection. This field involves analyzing nanoscale bioconvection mechanisms alongside viscous magnetohydrodynamic effects and has numerous applications, including smart coating technologies. Microorganisms can display gyrotactic, phototactic, chemotactic, and magnetotactic motions, each responsive to torque, light, chemicals, and magnetic fields. Biswas et al. [15] studied the magnetized movement of oxytactic microorganisms in a porous medium with copper nanoparticles suspended in a water-based nanofluid. Alhussain et al. [16] examined magnetic bioconvection nanofluid flow over a rotating cone using the Cattaneo—Christov heat flux model. Puneeth et al. [17] investigated bioconvection dynamics of a pseudoplastic nanofluid over a spinning cone. Mekheimer et al. [18] studied bioconvection-induced synovitis in blood flow with nanoparticles spreading across damaged tissues. Mahendra et al. [19] analyzed entropy generation and bioconvection in peristaltic nanofluid flow through an asymmetric channel using the Eyring—Powell model. Arain et al. [20] explored bioconvection in Sutterby fluid over a rotating disk in the presence of nanoparticles and an induced magnetic field, solving the nonlinear system using the DTM-Padé method.

In this study, synovial fluid is adopted as the non-Newtonian base fluid [21]. Synovial fluid acts as a lubricant and shock absorber within synovial joints. Due to its non-Newtonian nature, its viscosity decreases under shear, exhibiting shear-thinning behavior, which facilitates joint movement by reducing resistance and providing improved lubrication at rest. Synovial fluid also plays key roles in nutrient transport, waste removal, shock absorption, and lubrication. Its properties are crucial in diagnosing joint abnormalities [22, 23], such as inflammation, crystal deposition, and infections. Motivated by these applications, the primary objective of this work is to investigate the rheology of synovial fluid under bioconvection effects. The following sources [24-27] include contemporary research on bioconvection and nanofluid movement in different geometrical shapes.

The literature review highlights a gap in addressing this type of problem. The aim of the present study is to regulate the temperature of synovial fluid—responsible for lubricating joint movement within permeable knee cartilage—using magnetic fields, nanoparticles, and motile microorganisms. We solve the problem for two models: Model (1) exhibiting shear-thinning behavior and Model (2) exhibiting shear-thickening behavior. The coupled nonlinear system is solved numerically using the Runge—Kutta—Merson method combined with a finite difference scheme. We analyze the effects of velocity, temperature, nanoparticle concentration, and motile microorganism density on all the major physical parameters.

2. Problem Assumptions and Mathematical Model

An incompressible non-Newtonian synovial fluid fills the slender, flexible cylindrical tube that represents the studied arterial segment. Let (r', θ', z') denote the coordinates in the physical cylindrical polar coordinate system, with the z'-axis aligned along the artery axis and r', θ' corresponding to the radial and circumferential directions, respectively. We represent the temperature, concentration, and motile density at the endoscopic wall as T_0 , C_0 , N_0 , and at the outer wall as T_1 , T_2 , T_3 . A uniform magnetic field

B is applied along the perpendicular direction of the flow. We assume the geometrical structure to be porous, with a permeability of k. The mathematical representation of the artery geometry is detailed in Figure 1.

$$r' = \begin{cases} a_0 & \text{(endoscopewall),} \\ a_1 & \text{(arterywall),} \end{cases}$$
 (1)

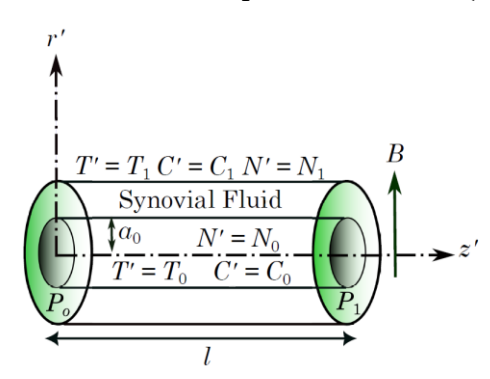


Figure 1: Geometry structure of synovial fluid flow through the artery under uniform magnetic field.

We investigate synovial fluid dynamics using a generalized incompressible non-Newtonian nanofluid model in which the viscosity depends on both shear rate and concentration. To incorporate the effects of hyaluronic acid concentration, an additional convection—diffusion equation is coupled with the system. Moreover, it is assumed that the swimming direction and velocity of the microorganisms are not influenced by the presence of nanoparticles in the fluid—an assumption that remains valid for dilute nanoparticle suspensions. The fundamental equations governing the flow of the synovial nanofluid are as follows:

Continuity equation:

$$\underline{\nabla}' \cdot \underline{V}' = 0. \tag{2}$$

Momentum equations:

$$\rho_{f}\left[\frac{\partial \underline{V'}}{\partial t'} + (\underline{V'} \cdot \underline{\nabla'})\underline{V'}\right] = -\underline{\nabla'}p' + \underline{J} \times \underline{B} + 2\underline{\nabla'} \cdot \mu'(C',\underline{\underline{D'}})\underline{\underline{D'}} - \frac{\mu}{k}\underline{V'}. \tag{3}$$

Energy equation:

$$(\rho c)_{f} \left[\frac{\partial T'}{\partial t'} + (\underline{V'} \cdot \underline{\nabla'}) T' \right] = k_{T} \nabla'^{2} T' + (\rho c)_{p} \left[\frac{D_{B}}{\Delta C'} (\underline{\nabla'} C' \cdot \underline{\nabla'} T') + \frac{D_{T}}{T_{m}} (\underline{\nabla'} T' \cdot \underline{\nabla'} T') \right]$$

$$+ \Phi + \frac{1}{\sigma'} \underline{J} \cdot \underline{J} + Q^{*} (T' - T_{0}).$$

$$(4)$$

Concentration equation:

$$\frac{\partial C'}{\partial t'} + (\underline{V'}, \underline{\nabla'})C' = \underline{\nabla'} \cdot (D_B \underline{\nabla'}C') + \frac{D_T}{T_m} \nabla'^2 T'. \tag{5}$$

Motile density equation:

$$\frac{\partial N'}{\partial t'} + (\underline{V'}.\underline{\nabla'})N' + \frac{bW_c}{c_1 - c_0}\underline{\nabla'} \cdot (N'\nabla'C') = D_m \nabla'^2 N'. \tag{6}$$

Corresponding slip boundary conditions:

$$w' = 0, \ T' = T_1, \ C' = C_1, \ N' = N_1, \ \text{at } r' = a_1,$$

$$\frac{\partial w'}{\partial r'} = -\frac{\alpha_1}{\sqrt{k}}(w' - w_p), \ T' = T_0, \ C' = C_0, \ N' = N_0, \ \text{at } r' = a_0,$$
(7)

where as μ' represents viscosity, $\underline{D'}$ denotes the symmetric part of the velocity gradient, ρ_f signifies the density of the base fluid, \underline{B} signifies the applied magnetic field, \underline{J} signifies the current density, ρ_p signifies the density of nanoparticles, $\underline{V'}$ signifies the velocity vector, N' stands for the density of motile microorganisms, p' signifies the pressure, Φ signifies the dissipation function, k_T signifies the thermal conductivity, Q^* signifies the heat source, T' signifies the temperature distribution, C' signifies the concentration of hyaluronan/hyaluronic, T_m signifies the mean temperature of the fluid, c_f signifies the heat capacity of the fluid, σ' signifies the electrical conductivity of the synovial fluid, c_p signifies the heat capacity of the nanoparticle, D_B signifies the Brownian diffusion coefficient, k signifies the permeability of porous, α_1 signifies the slip parameter, w_p signifies the Darcy velocity, b signifies the chemotaxis constant, W_c is a maximal cell speed, and D_T signifies the thermophoretic diffusion coefficient.

Let us focus on physical scenarios in which synovial fluid primarily exhibits viscous-like behavior. In such cases, the fluid behaves as an incompressible viscous medium, with viscosity varying according to the shear rate and hyaluronan concentration. In this investigation, we consider two synovial fluid models [28, 29], both exhibiting non-Newtonian behavior in two-dimensional flows.

Model (1): Viscosity is assumed to exhibit exponential dependence on the concentration

$$\mu'(C',\underline{\underline{D'}}) = e^{\alpha C'} (1 + \left|\underline{\underline{D'^2}}\right| \gamma^2)^n \mu_0, \tag{8}$$

Model (2): The shear thinning index is regarded as a function of concentration.

$$\mu'(C', \underline{D'}) = \mu_0 (1 + \left| \underline{D'^2} \right| \gamma^2)^{n(C')}, \tag{9}$$

In which

$$\left| \underline{\underline{D'}} \right| = \sqrt{2(\frac{\partial u'}{\partial r'})^2 + 2(\frac{u'}{r'})^2 + 2(\frac{\partial w'}{\partial z'})^2 + (\frac{\partial u'}{\partial z'} + \frac{\partial w'}{\partial r'})},\tag{10}$$

and

$$n(\mathcal{C}') = \frac{(1 - e^{-\alpha \mathcal{C}'})}{2},\tag{11}$$

where u', w' are the velocity components, n is the shear-thinning index ranging between -0.5 and 0, in which the model with n = 0.50 corresponds to a Newtonian fluid. The constants μ_0 , α , and γ are material constants. In order to streamline the mathematical modelling process, we convert all equations into a dimensionless configuration. To do this, we employ these dimensionless quantities:

$$r' = a_0 r, z' = lz, u' = \frac{a_0 u_0}{l} u, w' = u_0 w, \delta = \frac{a_0}{l}, t' = \frac{l}{u_0} t, \mu' = \mu \mu_0,$$

$$p' = \frac{u_0 l \mu_0}{a_0^2} p, \theta = \frac{T' - T_0}{T_1 - T_0}, \varphi = \frac{C' - C_0}{C_1 - C_0}, \chi = \frac{N' - N_0}{N_1 - N_0}, \underline{\underline{D}'} = \frac{u_0 \underline{\underline{D}}}{a_0},$$
(12)

By substituting the expression from Eq. (??) into Equations (2)-(11) and evaluating the conditions $R_e \le 0$ and $\delta \le 0$, the continuity Equation (2) is automatically fulfilled and the remaining equations are transformed as follows:

Momentum equations:

$$\frac{\partial p}{\partial r} = 0,\tag{13}$$

$$\frac{\partial p}{\partial z} = 2 \left[\frac{\mu}{r} \frac{\partial}{\partial r} \left(r \frac{\partial w}{\partial r} \right) + \frac{\partial \mu}{\partial r} \frac{\partial w}{\partial r} \right] - \sigma^2 \mu w - Hw. \tag{14}$$

Energy equation:

$$\frac{1}{r}\frac{\partial}{\partial r}\left(r\frac{\partial\theta}{\partial r}\right) + N_b\frac{\partial\theta}{\partial r}\frac{\partial\varphi}{\partial r} + N_t\left(\frac{\partial\theta}{\partial r}\right)^2 + E_cP_r\mu\left(\frac{\partial w}{\partial r}\right)^2 + E_cP_rHw^2 + E_cP_rQ\theta = 0.$$
(15)

Concentration equation:

$$\frac{1}{r}\frac{\partial}{\partial r}\left(r\frac{\partial\varphi}{\partial r}\right) + \frac{N_t}{N_h}\frac{1}{r}\frac{\partial}{\partial r}\left(r\frac{\partial\theta}{\partial r}\right) = 0. \tag{16}$$

Volume fraction:

$$\frac{1}{r}\frac{\partial}{\partial r}\left(r\frac{\partial\chi}{\partial r}\right) - P_e\frac{\partial}{\partial r}\left(\zeta\frac{\partial\varphi}{\partial r}\right) = 0,\tag{17}$$

and

$$\mu = (1 + \alpha \varphi) \left[1 + n w_e^2 \left(\frac{\partial w}{\partial r} \right)^2 \right], \qquad \text{Model(1)},$$

$$\mu = \left[1 + \frac{\alpha \varphi}{2} w_e^2 \left(\frac{\partial w}{\partial r} \right)^2 \right], \qquad \text{Model(2)}.$$
(18)

Corresponding boundary conditions

we 0,
$$\varphi = 1$$
, $\theta = 1$, $\chi = 1$ at $r = \epsilon = \frac{a_1}{a_0}$,

$$\frac{\partial w}{\partial r} = -\sigma \alpha_1 (w - w_p), \ \theta = 0, \ \chi = 0, \ \varphi = 0 \text{ at } r = 1.$$
(19)

The variables in the equation are defined as follows: N_t symbolizes the thermophoresis parameter, P_e symbolizes the Bioconvection Peclet number, σ symbolizes the porous parameter, P_r symbolizes the Prandtl number, N_b represents the Brownian motion parameter, H symbolizes the magnetic parameter, R_e symbolizes the Reynolds number, E_c symbolizes the Eckert number, Q symbolizes the heat source coefficient, and w_e symbolizes the synovial parameter. They are precisely and explicitly described as:

$$=\frac{(\rho c)_{p}D_{t}(T_{1}-T_{0})}{T_{m}k_{T}}, P_{e}=\frac{bW_{c}}{D_{m}}, \sigma=\frac{a_{0}}{\sqrt{k}}, N_{b}=\frac{(\rho c)_{p}D_{B}(C_{1}-C_{0})}{\Delta C'k_{T}}, Q=\frac{a_{0}^{2}Q^{*}}{u_{0}^{2}\mu_{0}}, H=\frac{\sigma B_{0}^{2}a_{0}^{2}}{\mu_{0}}, R_{e}=\frac{\rho_{f}u_{0}a_{0}}{\mu_{0}}, E_{c}$$

$$=\frac{u_{0}^{2}}{c_{f}(T_{1}-T_{0})}, w_{e}=\frac{\gamma u_{0}}{a_{0}}, P_{r}=\frac{\mu_{0}c_{f}}{k_{T}}$$

$$(20)$$

3. Numerical solution

3.1. Numerical Implementation using Finite Difference Discretization

The mathematical models (14)-(18), along with their boundary conditions, depict a nonlinear system with radial coordinates. As a result, analytical solutions are difficult to find, and numerical solutions are generated using FDM. To carry out the numerical scheme, the system is discretized using a second-order accurate finite difference approach devised in conservative cylindrical form. At each iteration, the discretization operation was conducted implicitly, using a tridiagonal process. The finished algebraic equations are iteratively solved using the Picard (fixed-point) technique. The detailed steps are listed below:

Radial Grid and Notations: The computational domain is divided into $\mathcal N$ uniform intervals in the following form as:

$$r_j = \varepsilon + j\Delta r, \quad j = 0, 1, \dots, \mathcal{N}, \quad \Delta r = \frac{1-\varepsilon}{\mathcal{N}}.$$
 (21)

The half-nodes are expressed as

$$r_{j+\frac{1}{2}} = \frac{(r_j + r_{j+1})}{2},$$
 (22)

The discretized form of first and second derivative for any scalar \mathcal{F} \mathscr{V} are approximated as:

$$(\mathcal{F}_r)_j \approx \frac{\mathcal{F}_{j+1} - \mathcal{F}_{j-1}}{2\Delta r},\tag{23}$$

$$(\mathcal{F}_r)_j \approx \frac{\mathcal{F}_{j+1} - \mathcal{F}_{j-1}}{2\Delta r},$$

$$\mathcal{L}_j[\mathcal{F}] \equiv \frac{1}{r_j} \frac{\mathcal{F}_{j+1} - \mathcal{F}_j}{\Delta r} - \frac{\mathcal{F}_i - \mathcal{F}_{j-1}}{2\Delta r}.$$

$$(23)$$

The above expression gives accurate representation of the second-order axisymmetric Laplacian operator. The weighted operator $\mathcal{L}_i^{\epsilon}[\mathcal{F}]$ for the variable-coefficient diffusion terms can be expressed as:

$$\mathcal{L}_{j}^{\epsilon}[\mathcal{F}] = \frac{1}{r_{i}} \frac{r_{j+\frac{1}{2}} \epsilon_{j+\frac{1}{2}} \epsilon_{j+\frac{1}{2}} \frac{\mathcal{F}_{j+1} - \mathcal{F}_{j}}{\Delta r} - r_{i-\frac{1}{2}} \epsilon_{i-\frac{1}{2}} \frac{\mathcal{F}_{j-1}}{\Delta r}}{\Delta r}, \tag{25}$$

where the transport coefficients is represented as $\epsilon_{j\pm\frac{1}{2}}$.

Discretization procedure: The momentum equation (14) can be articulated as

$$2 \mathcal{L}_{j}^{\mu}[w] - (\sigma^{2}\mu_{j} + H)w_{j} = \mathcal{P}, \qquad \mathcal{P} = \frac{\partial p}{\partial z}, \quad j = 1, \dots, \mathcal{N} - 1, \tag{26}$$

Discretization procedure: The momentum equation (14) can be articulated as
$$2 \mathcal{L}_{j}^{\mu}[w] - (\sigma^{2}\mu_{j} + H)w_{j} = \mathcal{P}, \qquad \mathcal{P} = \frac{\partial p}{\partial z}, \ j = 1, ..., \mathcal{N} - 1, \tag{26}$$
The derived tri-diagonal coefficients can be expressed in the following form:
$$\alpha_{j} = -\frac{2^{r} j - \frac{1}{2} \mu_{j} - \frac{1}{2}}{r_{j} \Delta r^{2}}, \qquad \beta_{j} = -\frac{2^{r} j + \frac{1}{2} \mu_{j} + \frac{1}{2}}{r_{j} \Delta r^{2}}, \tag{27}$$

$$\alpha_{j} = -\frac{2^{r} j + \frac{1}{2} \mu_{j} + \frac{1}{2} r_{j} - \frac{1}{2} \mu_{j} - \frac{1}{2}}{r_{j} \Delta r^{2}} + (\sigma^{2}\mu_{j} + H)$$

$$\gamma_{j} = \frac{{}^{2(r_{j+\frac{1}{2}\mu_{j+\frac{1}{2}}+r_{j-\frac{1}{2}\mu_{j-\frac{1}{2}})}}{r_{j}\Delta r^{2}} + (\sigma^{2}\mu_{j} + H). \tag{28}$$

The boundary conditions are as follows:

$$w_0 = 0, \quad \text{at} r = \varepsilon,$$
 (29)

$$\frac{w_{\mathcal{N}} - w_{\mathcal{N}-1}}{\Delta r} = -\sigma \alpha_1 (w_{\mathcal{N}} - w_p), \quad \text{at} r = 1, \tag{30}$$

that produces the discrete Robin condition
$$\frac{w_0 = 0, \quad \text{at} r = \varepsilon, \\
\frac{w_N - w_{N-1}}{\Delta r} = -\sigma \alpha_1 (w_N - w_p), \quad \text{at} r = 1, \\
(30)$$
that produces the discrete Robin condition
$$\left(-\frac{1}{\Delta r} - \sigma \alpha_1 \right) w_N + \frac{1}{\Delta r} w_{N-1} = -\sigma \alpha_1 w_p. \tag{31}$$
The France equation (15) can be discretized union the similar procedure as shown at each rode is and the prolinger

The Energy equation (15) can be discretized using the similar procedure as above at each node j, and the nonlinear terms are evaluated using the previous iterations:

$$\mathcal{L}_{j}[\theta] + Ec \, Pr \, Q \, \theta_{j}$$

$$= -[N_{b}(\theta_{r})_{j}^{nonlinear}(\varphi_{r})_{j}^{nonlinear} + N_{t}(\theta_{r}^{nonlinear})^{2},$$

$$+ Ec \, Pr \, \mu_{j}^{nonlinear}(w_{r}^{nonlinear})^{2} + Ec \, Pr \, H(w_{j}^{nonlinear})^{2}]. \tag{32}$$

The derived tri-diagonal coefficients can be expressed in the following form:

$$\alpha_j^e = -\frac{r_{j-\frac{1}{2}}}{r_j \Delta r^2}, \quad \gamma_i^e = -\frac{r_{j+\frac{1}{2}}}{r_j \Delta r^2}, \tag{33}$$

$$\beta_i^e = \frac{r_{j+\frac{1}{2}} + r_{j-\frac{1}{2}}}{r_i \Delta r^2} + Ec \, Pr \, Q. \tag{34}$$

The boundary conditions are as follows: $\theta_0 = 1$ at $r = \varepsilon$, $\theta_{\mathcal{N}} = 0$ at r = 1. The concentration equation (16) can be discretized using the similar procedure as above at each node j, we obtained: $\mathcal{L}_j[\varphi] = -\frac{N_t}{N_b} \mathcal{L}_j[\theta]^{nonlinear}. \tag{35}$ The derived tri-diagonal coefficients can be expressed similarly as the energy equation without the source term. The boundary

$$\mathcal{L}_{j}[\varphi] = -\frac{N_{t}}{N_{b}} \mathcal{L}_{j}[\theta]^{nonlinear}.$$
 (35)

conditions are as follows: $\varphi_0 = 1$ at $r = \varepsilon$, $\varphi_N = 0$ at r = 1.

The concentration equation (17) can be discretized using the similar procedure as above at each node j, we obtained:

$$\mathcal{L}_{j}[\chi] = P_{e} \frac{\zeta_{j+\frac{1}{2}} \frac{\varphi_{j+1} - \varphi_{j}}{\Delta r} - \zeta_{j-\frac{1}{2}} \frac{\varphi_{j} - \varphi_{j-1}}{\Delta r}}{\Delta r}.$$
(36)

 $\mathcal{L}_{j}[\chi] = P_{e} \frac{\zeta_{j+\frac{1}{2}} \frac{\varphi_{j+1} - \varphi_{j}}{\Delta r} - \zeta_{j-\frac{1}{2}} \frac{\varphi_{j} - \varphi_{j-1}}{\Delta r}}{\Delta r}.$ The boundary conditions are as follows: $\chi_{0} = 1$ at $r = \varepsilon$, $\chi_{\mathcal{N}} = 0$ at r = 1. At nodes and faces the nonlinear dynamics viscosity can be represented as:

 $\mu_{j+\frac{1}{2}} = \begin{cases} (1 + \alpha \varphi_{j+\frac{1}{2}}) \left[1 + n \, w_e^2 \, (w_r)_{j+\frac{1}{2}}^2 \right], & \text{Model(1),} \\ \alpha \varphi_{i+\frac{1}{2}} & w_e^2 \, (w_r)_{j+\frac{1}{2}}^2, & \text{Model(2).} \end{cases}$ (37)

The above set of equations are solved on computational software MALTAB using Picard algorithm. A comparison has been presented in Tables.

3.2. Rung-Kutta-Merson approach with Newton iteration

We utilize the Rung-Kutta-Merson approach with Newton iteration to effectively solve the system of nonlinear ordinary differential equations (13)-(19). The equations are solved through the shooting and matching procedure. When utilizing the shooting method, we rely on the D02HAF subroutine from the NAG Fortran library. This subroutine necessitates the provision of initial values for the absent initial and terminal conditions. The subroutine utilizes a sophisticated numerical method with adaptive step size to effectively manage the local truncation error. It then employs a well-known iterative technique to iteratively refine the estimated boundary values. You can find more information about the proposed numerical technique in these sources [30-32]. Below are some possible transformations:

$$w = Y_1, \qquad \theta = Y_3, \qquad \phi = Y_5, \qquad \zeta = Y_7. \tag{38}$$

 $w=Y_1, \qquad \theta=Y_3, \qquad \phi=Y_5, \qquad \zeta=Y_7.$ Equations (14)-(17) along with the boundary conditions (19) can be outlined in the following manner:

$$Y_1' = Y_2, \ 2(\mu Y_2' + \frac{\mu}{r} Y_2 + \mu' Y_2) - \sigma^2 Y_1 - H Y_1 = \frac{(P_0 - P_1)}{l},$$
 (39)

$$Y_3' = Y_4, \ Y_4' + \frac{1}{r}Y_4 + N_tY_4^2 + N_bY_4Y_6 + E_cP_rQY_3 + E_cP_r\mu Y_2^2 + E_cP_rHY_1^2 = 0, \tag{40}$$

$$Y_5' = Y_6,$$
 $Y_6' = -\frac{1}{r}Y_6 - \frac{(N_t)}{(N_b)}(Y_2' + \frac{1}{r}Y_2),$ (41)

$$Y_7' = Y_8,$$
 $Y_8' = -\frac{1}{r}Y_8 + P_e(Y_6Y_8 + Y_6'Y_7),$ (42)

with the following reduced boundary conditions:

$$Y_1 = 0$$
, $Y_3 = 1$, $Y_5 = 1$, and $Y_7 = 1$, at $r = \epsilon$,
 $Y_2 = -\sigma\alpha_1(Y_1 - w_p)$, $Y_3 = 0$, $Y_5 = 0$ and $Y_7 = 0$ at $r = 1$, (43)

where the prime demonstrates differentiation with regard to r. In order to calculate the physical quantities w, θ , φ and χ . The system of equations, labeled as Eqs. (39)-(42), is solved using Mathematica package version 9. The boundary conditions, labeled as (43), are also taken into consideration.

Table 1: Comparison of velocity and temperature profile with Finite difference approach.

r	w(r) (Present results)	$\theta(r)$ (Present results)	w(r) (FDM)	$\theta(r)$ (FDM)
1	0.841470985	0.540302306	0.84147	0.54030
1.026315789	0.855396474	0.517973814	0.85539	0.51797
1.052631579	0.868729618	0.495286635	0.86872	0.49528
1.078947368	0.881461183	0.47225648	0.88146	0.47225
1.105263158	0.893582353	0.448899296	0.89358	0.44889
1.131578947	0.905084735	0.425231257	0.90508	0.42523
1.157894737	0.915960363	0.401268755	0.91596	0.40126
1.184210526	0.926201706	0.377028381	0.92620	0.37702
1.210526316	0.935801672	0.352526923	0.93580	0.35252
1.236842105	0.944753613	0.327781346	0.94475	0.32778
1.263157895	0.95305133	0.302808787	0.95305	0.30280
1.289473684	0.960689078	0.277626539	0.96068	0.27762
1.315789474	0.967661567	0.25225204	0.96766	0.2522
1.342105263	0.973963969	0.226702861	0.97396	0.22670
1.368421053	0.979591919	0.200996695	0.97959	0.20099
1.394736842	0.984541521	0.175151342	0.98454	0.17515
1.421052632	0.988809347	0.149184701	0.98880	0.14918
1.447368421	0.992392441	0.123114752	0.99239	0.12311
1.473684211	0.995288323	0.096959548	0.99528	0.09695
1.5	0.997494987	0.070737202	0.99749	0.07073

Table 2: Comparison of concentration and microorganism profile with Finite difference approach.

r	$\phi(r)$ (Present results)	$\chi(r)$ (Present results)	$\phi(r)$ (FDM)	$\chi(r)$ (FDM)
1	1.557407725	0.693147181	1.55740	0.69314
1.026315789	1.651428028	0.706219262	1.65142	0.70621
1.052631579	1.753993661	0.719122667	1.75399	0.71912
1.078947368	1.866488278	0.731861693	1.86648	0.73186
1.105263158	1.990607609	0.744440475	1.99060	0.74444
1.131578947	2.128452975	0.756862995	2.12845	0.75686
1.157894737	2.282660566	0.769133088	2.28266	0.76913
1.184210526	2.456583514	0.781254448	2.45658	0.78125
1.210526316	2.654553769	0.793230639	2.65455	0.79323
1.236842105	2.882267779	0.805065097	2.88226	0.80506
1.263157895	3.147370122	0.816761137	3.14737	0.81676
1.289473684	3.460364706	0.828321959	3.46036	0.82832
1.315789474	3.836090152	0.839750655	3.83609	0.83975
1.342105263	4.296213835	0.85105021	4.29621	0.8510
1.368421053	4.873671776	0.862223511	4.87367	0.86222
1.394736842	5.621090355	0.873273347	5.62109	0.87327
1.421052632	6.628088147	0.884202417	6.62808	0.88420
1.447368421	8.060711066	0.895013333	8.06071	0.89501
1.473684211	10.26498518	0.905708623	10.2649	0.90570
1.5	14.10141995	0.916290732	14.1014	0.91629

4. Graphical Results and Discussion

The present study employs a combination of the shooting method and the Runge–Kutta–Merson scheme to analyze and present the results. This section provides a detailed discussion of the key physical parameters—velocity, temperature, nanoparticle concentration, and the density of motile microorganisms. To illustrate these effects, we include graphical representations showing how variations in specific parameters influence the flow of synovial fluid within permeable knee cartilage for both the shear-thinning Model (1) and the shear-thickening Model (2). The effects of all parameters are depicted in Figures 2–18. In addition, Tables 1 and 2 provide numerical comparisons obtained using the finite difference method, confirming that the present results show excellent agreement with the proposed methodology.

Figure 2–6 illustrate how various emerging parameters influence the flow velocity. Figure 2 shows the effect of the magnetic parameter H on velocity for both the shear-thinning and shear-thickening models of synovial fluid. The graph clearly reveals that the velocity decreases as H increases for both models, with the shear-thinning model exhibiting comparatively higher velocity. Figure 3 presents the influence of the concentration production parameter α on the velocity distribution. This parameter significantly enhances the velocity profile. It is also observed that the flow rate is higher under no-slip conditions than under slip conditions.

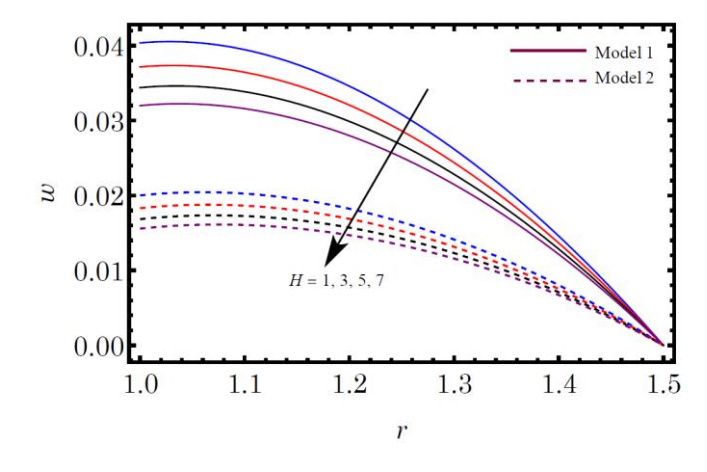
Figure 4 compares the velocity profiles of a Newtonian fluid and synovial fluid for varying values of the pressure parameter P_o . The results indicate that the velocity is higher in synovial fluid, with the maximum velocity occurring near the surface of the knee cartilage. Figure 5 demonstrates the changes in velocity due to variations in the porous parameter σ and the slip parameter α_1 . Higher values of σ and α_1 lead to a reduction in velocity. Finally, Figure 6 shows the effects of Darcy velocity w_p and the synovial fluid parameter w_e on the velocity profiles. An apparent decrease in fluid activity is observed as w_p increases. Although the synovial parameter w_e also causes a reduction in velocity, its influence is relatively minor.

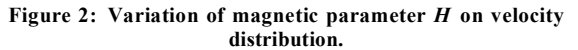
Figure 7 presents the influence of the pressure parameter P_o on the fluid temperature for Models (1) and (2). The temperature profile increases with rising P_o in both models; however, the upward trend is more pronounced in Model (1). Figure 8 illustrates the effect of the heat source parameter Q on the temperature of Newtonian and synovial fluids containing nanoparticles and microorganisms. The results show that increasing Q enhances the temperature in all cases, with a significantly higher temperature observed in synovial fluid containing both nanoparticles and microbes.

Figure 9 displays the impact of the concentration production parameter α on the temperature of synovial fluid with and without nanoparticles and microorganisms. It is evident that the temperature increases in both cases, although the enhancement is more prominent for synovial fluid containing nanoparticles and microorganisms. Figure 10 shows how the Brownian motion parameter N_b and the thermophoresis parameter N_t influence temperature distribution. The figure clearly demonstrates that increases in both N_b and N_t lead to notable rises in temperature. Physically, higher Brownian motion reflects intensified random movement of nanoparticles, which generates additional thermal energy. Similarly, larger values of N_t imply stronger thermophoretic forces that drive nanoparticles away from the heated surface, altering the thermal gradient and contributing to temperature elevation.

Figure 11 illustrates the effects of the Eckert number E_c and the Prandtl number P_r on temperature. Both parameters are found to increase the temperature of the fluid, indicating their significant role in enhancing thermal energy within the system.

Figure 12 analyzes the effect of the pressure parameter P_0 on the nanoparticle concentration for both the shear-thinning Model (1) and the shear-thickening Model (2). The results reveal that the pressure generated by the motion of synovial fluid containing nanoparticles and microorganisms effectively reduces the nanoparticle concentration. Furthermore, the concentration in Model (1) is lower than in Model (2). Figure 13 compares the nanoparticle concentration in Newtonian fluid and synovial fluid in the presence of the heat source parameter Q, along with microorganisms. It is observed that increasing Q leads to a rise in nanoparticle concentration in both cases, although the concentration profile is slightly lower in synovial fluid compared to the Newtonian fluid.





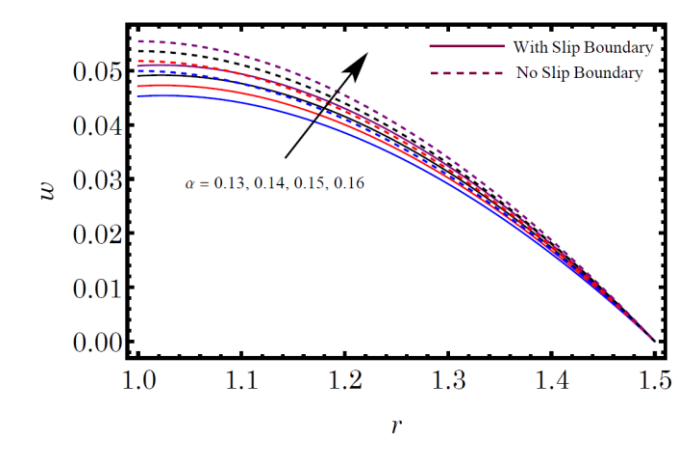
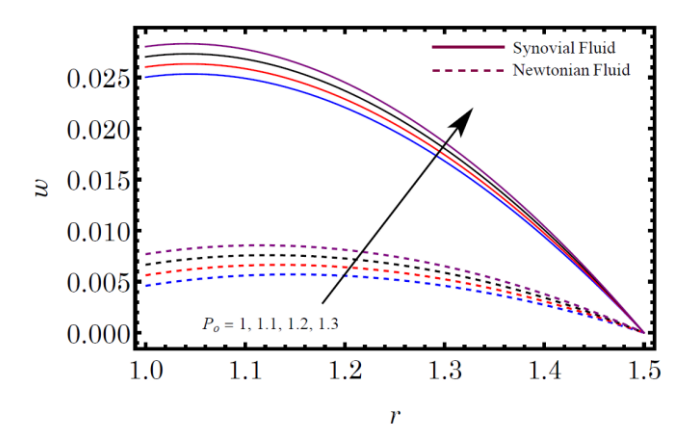


Figure 3: Variation of concentration production α on velocity distribution.

Figure 14 illustrates the influence of the concentration production parameter α on the nanoparticle concentration in synovial fluid with and without nanoparticles and microorganisms. The graph clearly shows that increasing α decreases nanoparticle concentration in both scenarios. When nanoparticles and microorganisms are present, their combined effect leads to a more significant change in the concentration profile; however, in their absence, the change in synovial fluid is minimal. Figure 15 examines the effects of the thermophoresis parameter N_t and the Brownian motion parameter N_t on nanoparticle concentration. The figure demonstrates that nanoparticle concentration decreases with increasing N_t , while the opposite trend is observed with increasing N_t .

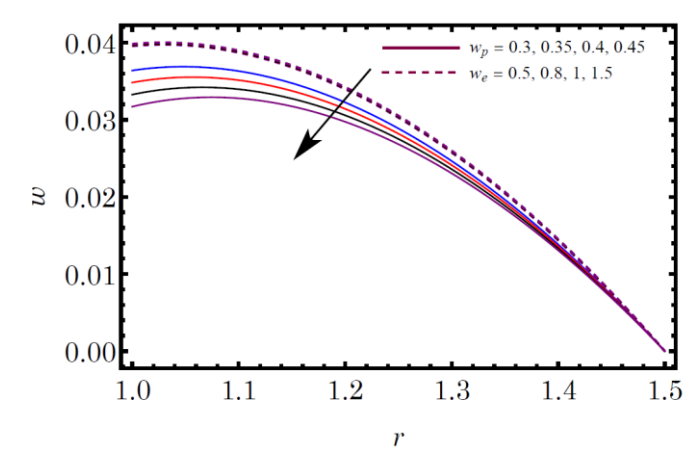
Figure 16 illustrates the variation in the density of motile microorganisms as the heat source parameter Qchanges. This analysis considers both Newtonian fluid and synovial fluid containing nanoparticles and microorganisms. The results show that the heat source associated with fluid motion reduces the density of motile microbes. Additionally, the density of motile microorganisms is higher in Newtonian fluid compared to synovial fluid. Figure 17 presents the effects of the thermophoresis parameter N_t and the Brownian motion parameter N_b on the density of motile microorganisms. Increasing N_t decreases microbial density, whereas increasing N_b produces the opposite effect. Figure 18 examines the relationship between the pressure parameter P_o and the bioconvection Peclet number P_e with respect to microorganism density. The visualization clearly shows that increases in both P_o and P_e lead to a decline in the density of motile microorganisms.

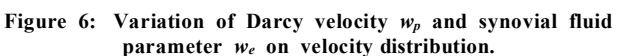


0.04 0.03 0.02 0.01 0.00 1.0 1.1 1.2 1.3 1.4 1.5

Figure 4: Variation of pressure variation P_o on velocity distribution.

Figure 5: Variation of slip parameter α_1 and porous parameter σ on velocity distribution.





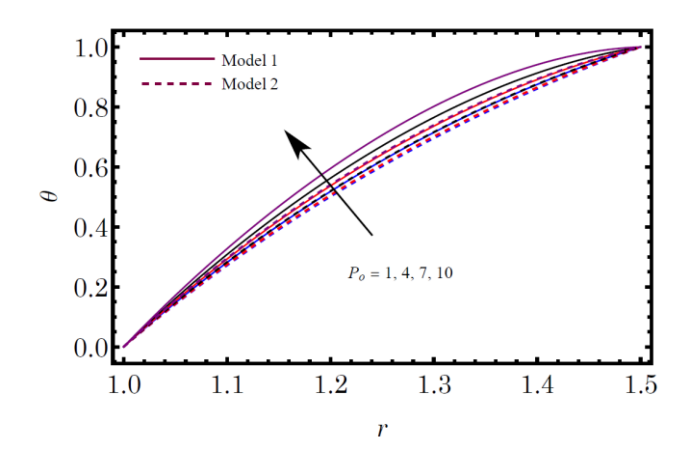
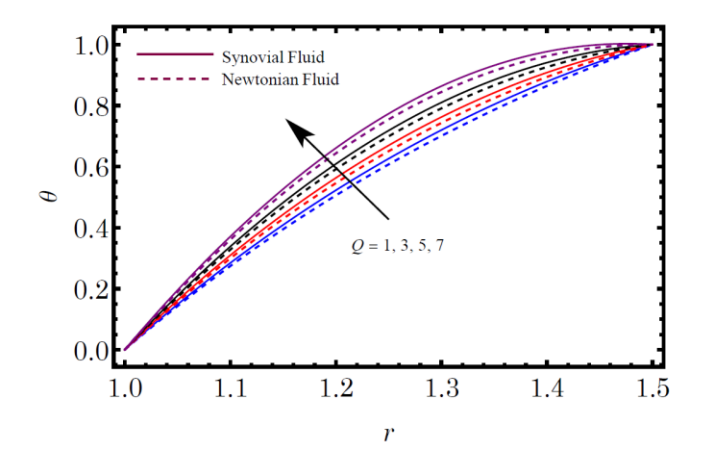


Figure 7: Variation of pressure variation P_o on temperature distribution.



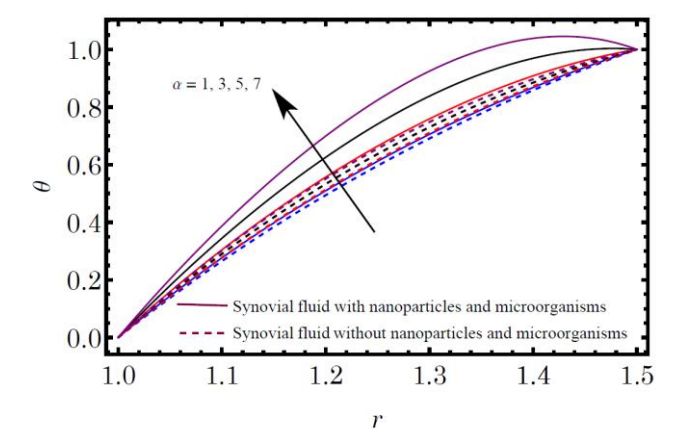
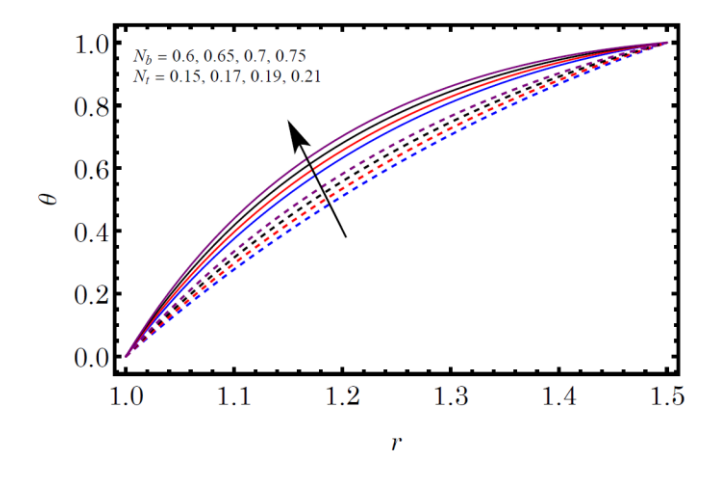


Figure 8: Variation of heat source ${\it Q}$ on temperature distribution.

Figure 9: Variation of concentration production α on temperature distribution.



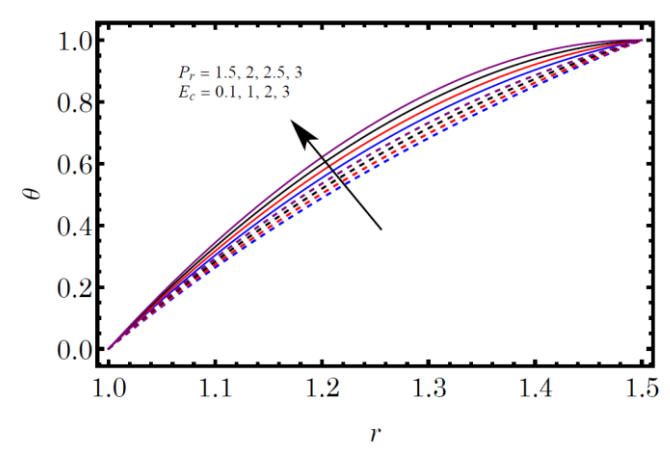
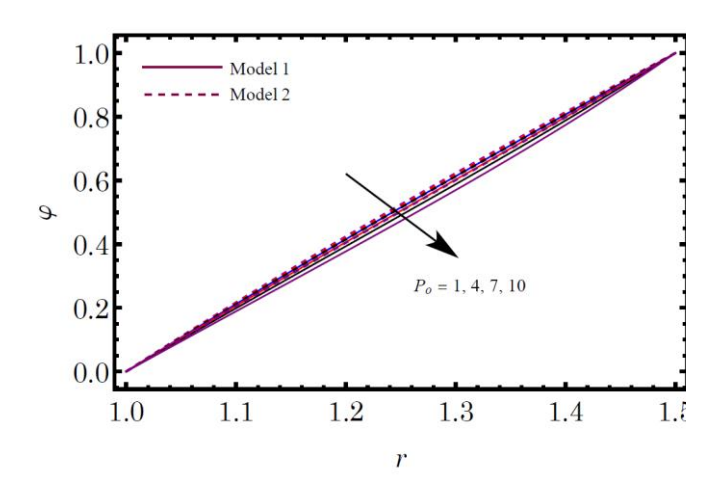


Figure 10: Variation of Brownian motion N_b and thermophoresis N_t parameter on temperature distribution.

Figure 11: Variation of Eckert number E_c and Prandtl number P_r on temperature distribution.



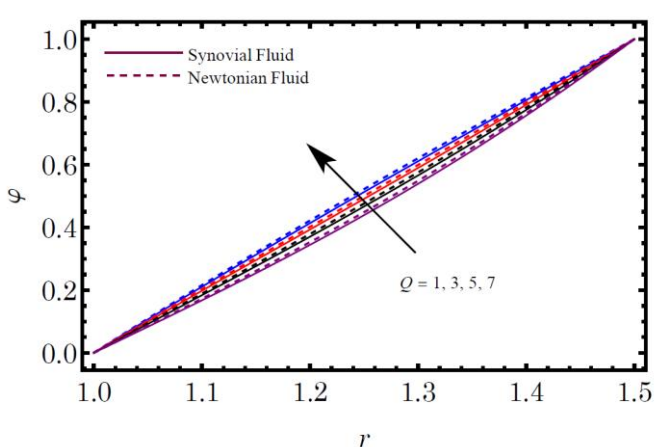
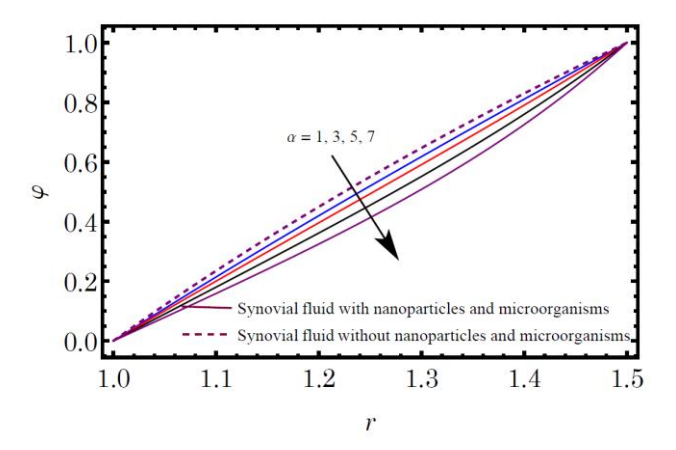
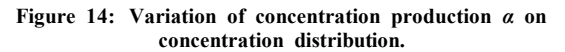


Figure 12: Variation of pressure variation P_o on concentration distribution.

Figure 13: Variation of heat source Q on concentration distribution.





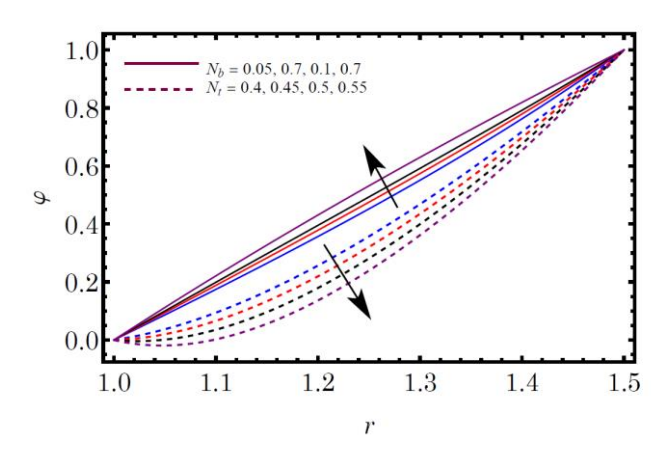


Figure 15: Variation of Brownian motion N_b and thermophoresis N_t parameter on concentration distribution.

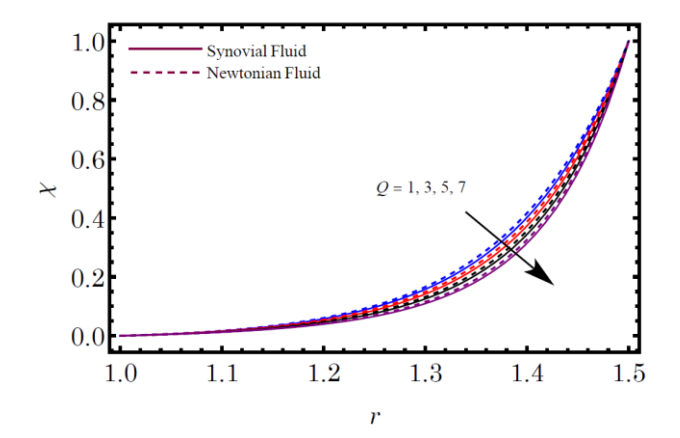


Figure 16: Variation of heat source *Q* on motile microorganism distribution.

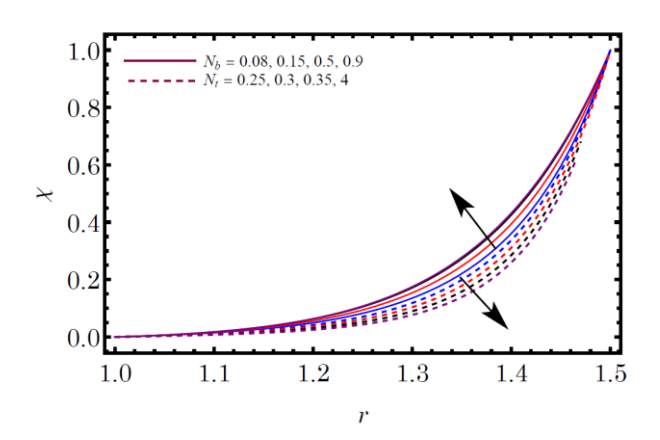


Figure 17: Variation of Brownian motion N_b and thermophoresis N_t parameter on motile microorganism distribution.

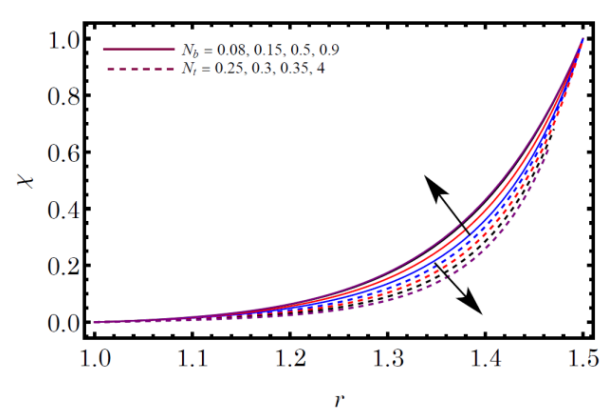


Figure 18: Variation of pressure variation P_o and bioconvection Peclet number P_e on motile microorganism distribution.

5. Concluding remarks

In the present study, we investigated the bioconvection of synovial fluid flowing through porous knee cartilage, incorporating the effects of magnetic fields and porosity. The mathematical formulation was examined for two rheological models: Model (1), exhibiting shear-thinning behavior, and Model (2), exhibiting shear-thickening behavior. To solve the nonlinear system, we employed the Runge–Kutta–Merson algorithm combined with shooting techniques. The key findings of this investigation are summarized below:

i. An increase in the magnetic field strength leads to a reduction in velocity for both models, with higher velocities observed in the shear-thinning case.

- ii. The velocity distribution is enhanced by increasing the concentration production parameter and the slip parameter.
- iii. Velocity increases when synovial fluid is considered, with the maximum velocity occurring at the knee cartilage surface.
- iv. The thermal profile of Model (1) exhibits a higher magnitude compared to Model (2).
- v. The heat source parameter elevates the temperature for both fluid types, with synovial fluid showing a more pronounced increase than Newtonian fluid.
- vi. The concentration production parameter enhances the temperature profile regardless of the presence of nanoparticles and microorganisms.
- vii. The Prandtl number, Brownian motion parameter, Eckert number, and thermophoresis parameter all have significant effects on the temperature distribution.
- viii. The pressure generated by synovial fluid motion, when combined with nanoparticles and microorganisms, reduces the nanoparticle concentration.
 - ix. Nanoparticle concentration is lower in Model (1) than in Model (2).
 - x. The presence of a heat source increases nanoparticle concentration in both fluid types.
- xi. The nanoparticle concentration decreases with increasing thermophoresis parameter N_t , while the Brownian motion parameter N_b produces the opposite effect.
- xii. The heat source associated with fluid motion decreases the density of motile microorganisms.
- xiii. A higher thermophoresis parameter further reduces microorganism density, whereas an increase in Brownian motion leads to a rise in microorganism density.
- xiv. The density of motile microorganisms decreases as the bioconvection Peclet number increases.

5.1. Limitations and proposed future work

This study is primarily theoretical, aimed at developing a fundamental understanding of bioconvection and thermal transport phenomena in nanofluids using a synovial fluid model. Although we highlight potential biomedical applications—such as joint lubrication and targeted drug delivery—we do not address the practical challenges associated with real-world implementation, including cost, scalability, and safety. Future work may include experimental validation and the exploration of applications in clinical systems, implantable devices, and industrial thermal management technologies.

While the mechanical effects of nanoparticle transport are not modeled in this study, it is important to acknowledge that nanoparticles may contribute to wear or corrosion of system components, such as pipes and heat exchangers, due to their small size and abrasive properties. Future investigations could examine the long-term implications of these effects and evaluate mitigation strategies, including the use of protective coatings or corrosion-resistant materials.

Moreover, the economic viability of nanofluid technologies at large scales remains a challenge, particularly with regard to maintaining long-term stability. Developing open-access synthesis protocols and establishing standardized quality control measures could help lower production costs and improve reproducibility, thereby making the technology more accessible for industrial and biomedical applications.

Finally, although our model focuses on controlled biomedical environments, potential risks associated with nanoparticle leakage or improper disposal merit further investigation. Future research could incorporate environmental modeling to assess nanoparticle dispersion, evaluate potential toxicity, and inform safe handling and disposal practices.

References

- [1] J. C. Maxwell, 1873, A treatise on electricity and magnetism, Oxford: Clarendon Press,
- [2] S. U. Choi, Enhancing thermal conductivity of fluids with nanoparticles, in *Proceeding of,* American Society of Mechanical Engineers, pp. 99-105.
- [3] C. E. Lee, Rapid and repeated invasions of fresh water by the copepod Eurytemora affinis, *Evolution*, Vol. 53, No. 5, pp. 1423-1434, 1999, 1999.
- [4] K. V. Wong, O. De Leon, Applications of nanofluids: current and future, *Advances in mechanical engineering*, Vol. 2, pp. 519659, 2010, 2010.
- [5] A. Imran, R. Akhtar, Z. Zhiyu, M. Shoaib, M. A. Z. Raja, Heat transfer analysis of biological nanofluid flow through ductus efferentes, *AIP Advances*, Vol. 10, No. 3, 2020, 2020.
- [6] M. R. Eid, Effects of NP shapes on non-Newtonian bio-nanofluid flow in suction/blowing process with convective condition: Sisko model, *Journal of Non-Equilibrium Thermodynamics*, Vol. 45, No. 2, pp. 97-108, 2020, 2020.
- [7] A. F. Elelamy, N. S. Elgazery, R. Ellahi, Blood flow of MHD non-Newtonian nanofluid with heat transfer and slip effects: Application of bacterial growth in heart valve, *International Journal of Numerical Methods for Heat & Fluid Flow,* Vol. 30, No. 11, pp. 4883-4908, 2020, 2020.
- [8] M. M. Bhatti, A. Riaz, L. Zhang, S. M. Sait, R. Ellahi, Biologically inspired thermal transport on the rheology of Williamson hydromagnetic nanofluid flow with convection: an entropy analysis, *Journal of Thermal Analysis and Calorimetry*, Vol. 144, pp. 2187-2202, 2021, 2021.
- [9] K. Elangovan, K. Subbarao, K. Gangadhar, An analytical solution for radioactive MHD flow TiO2–Fe3O4/H2O nanofluid and its biological applications, *International Journal of Ambient Energy*, Vol. 43, No. 1, pp. 7576-7587, 2022, 2022.
- [10] B. K. Sharma, U. Khanduri, N. K. Mishra, K. S. Mekheimer, Combined effect of thermophoresis and Brownian motion on MHD mixed convective flow over an inclined stretching surface with radiation and chemical reaction, *International Journal of Modern Physics B*, Vol. 37, No. 10, pp. 2350095, 2023, 2023.

- [11] Q. Raza, X. Wang, M. Z. A. Qureshi, S. M. Eldin, A. M. Abd Allah, B. Ali, I. Siddique, Mathematical modeling of nanolayer on biological fluids flow through porous surfaces in the presence of CNT, *Case Studies in Thermal Engineering*, Vol. 45, pp. 102958, 2023, 2023.
- [12] A. V. Kuznetsov, The onset of thermo-bioconvection in a shallow fluid saturated porous layer heated from below in a suspension of oxytactic microorganisms, *European Journal of Mechanics-B/Fluids*, Vol. 25, No. 2, pp. 223-233, 2006, 2006.
- [13] A. V. Kuznetsov, The onset of nanofluid bioconvection in a suspension containing both nanoparticles and gyrotactic microorganisms, *International Communications in Heat and Mass Transfer*, Vol. 37, No. 10, pp. 1421-1425, 2010, 2010.
- [14] H. T. Basha, R. Sivaraj, Numerical simulation of blood nanofluid flow over three different geometries by means of gyrotactic microorganisms: applications to the flow in a circulatory system, *Proceedings of the Institution of Mechanical Engineers, Part C: Journal of Mechanical Engineering Science*, Vol. 235, No. 2, pp. 441-460, 2021, 2021.
- [15] N. Biswas, N. K. Manna, D. K. Mandal, R. S. R. Gorla, Magnetohydrodynamic bioconvection of oxytactic microorganisms in porous media saturated with Cu–water nanofluid, *International Journal of Numerical Methods for Heat & Fluid Flow*, Vol. 31, No. 11, pp. 3461-3489, 2021, 2021.
- [16] Z. A. Alhussain, A. Renuka, M. Muthtamilselvan, A magneto-bioconvective and thermal conductivity enhancement in nanofluid flow containing gyrotactic microorganism, *Case Studies in Thermal Engineering*, Vol. 23, pp. 100809, 2021, 2021.
- [17] V. Puneeth, M. Sarpabhushana, M. S. Anwar, E. H. Aly, B. J. Gireesha, Impact of bioconvection on the free stream flow of a pseudoplastic nanofluid past a rotating cone, *Heat Transfer*, Vol. 51, No. 5, pp. 4544-4561, 2022, 2022.
- [18] K. S. Mekheimer, R. E. Abo-Elkhair, S. I. Abdelsalam, K. K. Ali, A. M. A. Moawad, Biomedical simulations of nanoparticles drug delivery to blood hemodynamics in diseased organs: Synovitis problem, *International Communications in Heat and Mass Transfer*, Vol. 130, pp. 105756, 2022, 2022.
- [19] D. L. Mahendra, J. U. Viharika, V. Ramanjini, O. D. Makinde, U. B. Vishwanatha, Entropy analysis on the bioconvective peristaltic flow of gyrotactic microbes in Eyring-Powell nanofluid through an asymmetric channel, *Journal of the Indian Chemical Society*, Vol. 100, No. 3, pp. 100935, 2023, 2023.
- [20] M. B. Arain, A. Zeeshan, M. M. Bhatti, M. S. Alhodaly, R. Ellahi, Description of non-Newtonian bioconvective Sutterby fluid conveying tiny particles on a circular rotating disk subject to induced magnetic field, *Journal of Central South University*, Vol. 30, No. 8, pp. 2599-2615, 2023, 2023.
- [21] H. Fam, J. T. Bryant, M. Kontopoulou, Rheological properties of synovial fluids, *Biorheology*, Vol. 44, No. 2, pp. 59-74, 2007, 2007.
- [22] A. Swan, H. Amer, P. Dieppe, The value of synovial fluid assays in the diagnosis of joint disease: a literature survey, *Annals of the rheumatic diseases*, Vol. 61, No. 6, pp. 493-498, 2002, 2002.
- [23] L. Ben-Trad, C. I. Matei, M. M. Sava, S. Filali, M.-E. Duclos, Y. Berthier, M. Guichardant, N. Bernoud-Hubac, O. Maniti, A. Landoulsi, others, Synovial extracellular vesicles: Structure and role in synovial fluid tribological performances, *International Journal of Molecular Sciences*, Vol. 23, No. 19, pp. 11998, 2022, 2022.
- [24] U. Khanduri, B. K. Sharma, B. Almohsen, M. M. Bhatti, Electroosmotic and Gyrotactic Microorganisms Effects on MHD Al₂O₃-Cu/Blood Hybrid Nanofluid Flow through Multi-Stenosed Bifurcated Artery, *Frontiers in Bioscience-Landmark*, Vol. 29, No. 3, pp. 110, 2024, 2024.
- [25] A. Yusuf, S. U. Khan, M. Hassan, M. M. Bhatti, H. F. Öztop, Heat transfer optimization of MWCNT-Al2O3 hybrid nanofluids under convective and irreversible effects, *Journal of Umm Al-Qura University for Applied Sciences*, pp. 1-15, 2025, 2025.
- [26] S. U. Khan, S. Bibi, A. Bibi, K. B. Saleem, B. M. Alshammari, R. Hajlaoui, L. Kolsi, Evaluation of thermal bioconvective phenomenon for periodically accelerating nonlinear radiated flow of Maxwell nanofluid with triple diffusion effects, *Alexandria Engineering Journal*, Vol. 93, pp. 22-32, 2024, 2024.
- [27] E. E. Bafe, M. D. Firdi, L. G. Enyadene, Magnetohydrodynamic thermo-bioconvective flow of 3D rotating Williamson nanofluid with Arrhenius activation energy in a Darcy–Forchheimer medium over an exponentially stretching Surface, *International Journal of Thermofluids*, Vol. 21, pp. 100585, 2024, 2024.
- [28] B. Rothammer, M. Marian, F. Rummel, S. Schroeder, M. Uhler, J. P. Kretzer, S. Tremmel, S. Wartzack, Rheological behavior of an artificial synovial fluid–influence of temperature, shear rate and pressure, *Journal of the Mechanical Behavior of Biomedical Materials*, Vol. 115, pp. 104278, 2021, 2021.
- [29] J. Liao, S. Miramini, X. Liu, L. Zhang, Computational study on synovial fluid flow behaviour in cartilage contact gap under osteoarthritic condition, *Computers in Biology and Medicine*, Vol. 123, pp. 103915, 2020, 2020.
- [30] E. Loghman, A. Kamali, F. Bakhtiari-Nejad, M. Abbaszadeh, M. Amabili, On the combined Shooting-Pseudo-Arclength method for finding frequency response of nonlinear fractional-order differential equations, *Journal of Sound and Vibration*, Vol. 516, pp. 116521, 2022, 2022.
- [31] C.-S. Liu, C.-W. Chang, Periodic solutions of nonlinear ordinary differential equations computed by a boundary shape function method and a generalized derivative-free Newton method, *Mechanical Systems and Signal Processing*, Vol. 184, pp. 109712, 2023, 2023.
- [32] J. H. Z. Q. Zhou, Y. G. Zhao, Nonlinear buckling and postbuckling of circular plates reinforced with graphene platelets using the shooting method, *Journal of Structural Stability and Dynamics* Vol. 24, No. 1, pp. 2450001, 2024.